C. R. Physique 15 (2014) 616–629

Contents lists available at ScienceDirect

Comptes Rendus Physique

www.sciencedirect.com

Emergent phenomena in actinides / Phénomènes émergents dans les actinides

Fermi surface, magnetic, and superconducting properties in actinide compounds

Surface de Fermi, magnétisme et supraconductivité dans les composés d'actinides

Yoshichika Ōnuki [a,*], Rikio Settai [b], Yoshinori Haga [c], Yo Machida [d], Koichi Izawa [d], Fuminori Honda [e], Dai Aoki [e,f]

[a] *Faculty of Science, University of the Ryukyus, Nishihara, Okinawa 903-0213, Japan*
[b] *Department of Physics, Faculty of Science, Niigata University, Niigata 950-2181, Japan*
[c] *Advanced Science Research Center, Japan Atomic Energy Agency, Tokai, Ibaraki 319-1195, Japan*
[d] *Department of Physics, Tokyo Institute of Technology, Meguro 152-8551, Japan*
[e] *Institute for Materials Research, Tohoku University, Oarai, Ibaraki 311-1313, Japan*
[f] *SPSMS, UMR-E CEA, UJF-Grenoble 1, INAC, 38054 Grenoble, France*

ARTICLE INFO

Article history:
Available online 24 July 2014

Keywords:
Fermi surface
Heavy fermion
Anisotropic superconductivity
UPt_3
$NpPd_5Al_2$
UGe_2

Mots-clés :
Surface de Fermi
Fermion lourds
Supraconductivité anisotrope
UPt_3
$NpPd_5Al_2$
UGe_2

ABSTRACT

The de Haas–van Alphen effect, which is a powerful method to explore Fermi surface properties, has been observed in cerium, uranium, and nowadays even in neptunium and plutonium compounds. Here, we present the results of several studies concerning the Fermi surface properties of the heavy fermion superconductors UPt_3 and $NpPd_5Al_2$, and of the ferromagnetic pressure-induced superconductor UGe_2, together with those of some related compounds for which fascinating anisotropic superconductivity, magnetism, and heavy fermion behavior has been observed.

RÉSUMÉ

L'effet de Haas–van Alphen, une méthode puissante pour explorer les propriétés de la surface de Fermi dans les solides, a été observé dans de nombreux composés du cérium, de l'uranium, du neptunium et du plutonium. Dans cet article, on présente les résultats obtenus pour les supraconducteurs à fermions lourds UPt_3 et $NpPd_5Al_2$, ainsi que pour le composé UGe_2 qui, soumis à une pression externe, devient supraconducteur en présence d'ordre ferromagnétique. On considère aussi certains systèmes analogues caractérisés par des états électroniques remarquables (supraconductivité anisotrope, magnétisme et comportement à fermions lourds).

* Corresponding author.
E-mail address: onuki@phys.u-ryukyu.ac.jp (Y. Ōnuki).

http://dx.doi.org/10.1016/j.crhy.2014.06.005
1631-0705/

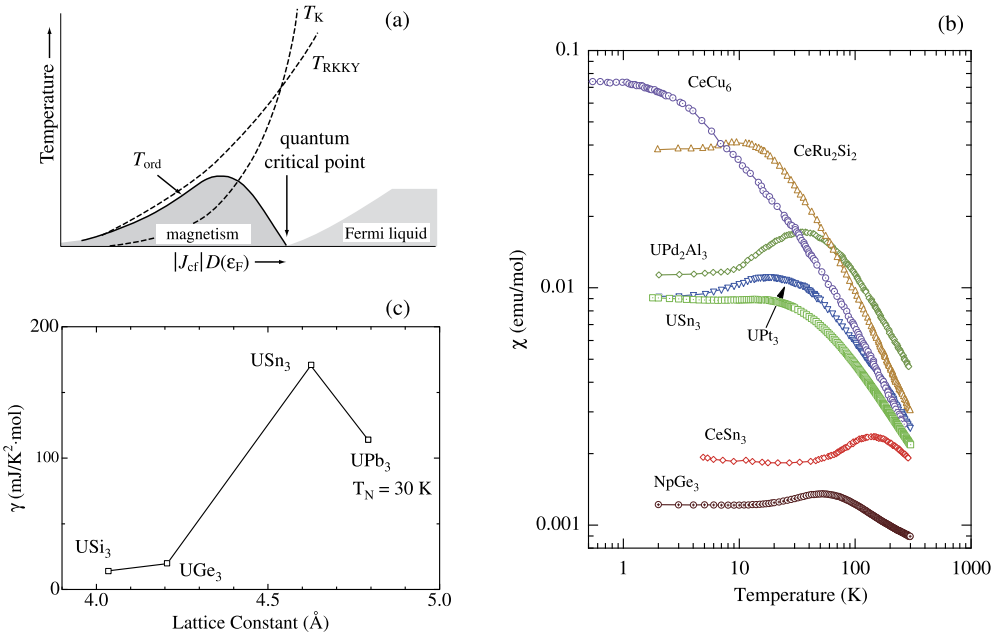

Fig. 1. (Color online.) (a) Doniach phase diagram, (b) the temperature dependence of the magnetic susceptibility in cerium, uranium and transuranium compounds, and (c) the γ vs lattice constant in UX_3 (X: Si, Ge, Sn, and Pb), cited from Ref. [5].

1. Introduction

In the presence of a strong magnetic field H, conduction electrons describe cyclotron orbits with discrete energy values, the so-called Landau levels. As the intensity of the magnetic field is increased, Landau levels cross the Fermi energy and the magnetic moment of the metal oscillates with a frequency F $(= c\hbar S_F/2\pi e)$ proportional to the extreme (maximum or minimum) cross-sectional area S_F of the Fermi surface. This is the well-known de Haas–van Alphen (dHvA) effect, a powerful method to image the Fermi surface and determine the effective cyclotron mass m_c^* and the scattering lifetime τ of conduction electrons. Magnetic moment oscillations are measured as a function of the magnetic field for different orientations of the sample, and from the angular dependence of the dHvA frequency f, obtained by fast Fourier transformation (FFT) of the oscillation curves, the topology of the Fermi surface can be determined with the help of energy-band calculations. The dHvA effect was first studied for the s and p electron systems, then for interacting electron systems based on the transition metal compounds, and eventually extended to strongly correlated electron systems of rare earth, uranium, and transuranium compounds [1–3].

The f electrons of cerium, ytterbium, uranium and transuranium compounds exhibit a variety of characteristic features, including spin and charge orderings, spin and valence fluctuations, heavy fermion and anisotropic (unconventional) superconductivity [1–3]. This variety is the result of the competition between the Ruderman–Kittel–Kasuya–Yosida (RKKY) interaction and the Kondo effect, as discussed by Doniach [4] and shown schematically in Fig. 1(a) as a function of $|J_{cf}|D(\varepsilon_F)$. $|J_{cf}|$ is the magnetic exchange interaction between conduction and f electrons, and $D(\varepsilon_F)$ is the density of states at the Fermi energy ε_F. The Doniach phase diagram is a good guiding principle to reach the quantum critical point (QCP), which is defined as the magnetic ordering temperature $T_{ord} \to 0$. Experimentally, $|J_{cf}|D(\varepsilon_F)$ is replaced by pressure P, and $T_{ord} \to 0$ is reached for $P \to P_c$ (P_c being the critical pressure). The heavy fermion state is formed in the QCP region.

The magnetic susceptibility χ of $CeCu_6$ and $CeRu_2Si_2$, as well as that of UPt_3, shown in Fig. 1(b), increases with decreasing temperature, following the Curie–Weiss law at high temperatures, and has a maximum at a characteristic temperature $T_{\chi max}$. Below $T_{\chi max}$, the susceptibility becomes almost temperature-independent, and the f-electron system is changed into a new electronic state, called the heavy fermion state. Here, $T_{\chi max}$ approximately corresponds to the Kondo temperature T_K [5].

The heavy fermion state in the cerium compound is understood as follows. At low temperatures, the magnetic entropy of the ground-state doublet in the crystal electric field (CEF) scheme of the 4f levels, $R\ln 2$, is obtained by integrating the magnetic specific heat C_m in the form of C_m/T over the temperature. When C_m is changed into the electronic specific heat γT via the many-body Kondo effect, the following relations are obtained:

$$R\ln 2 = \int_0^{T_K} \frac{C_m}{T}\,dT \tag{1}$$

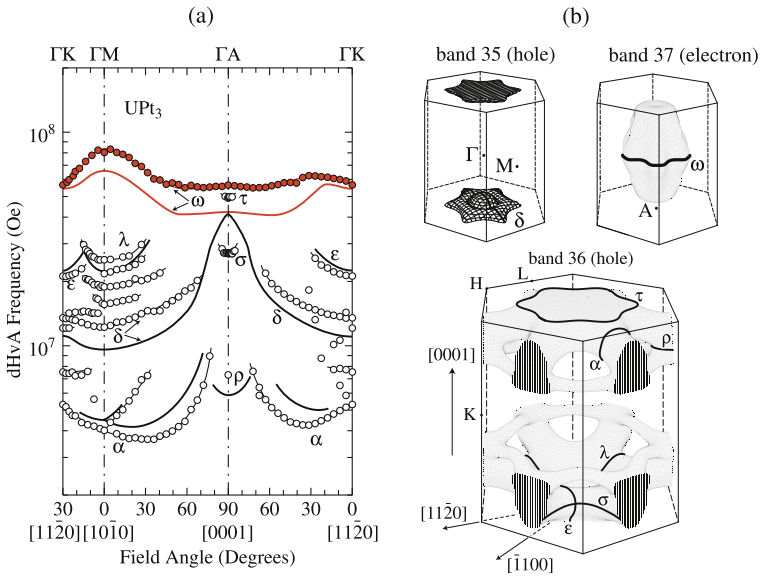

Fig. 2. (Color online.) (a) Angular dependencies of the dHvA frequencies in UPt_3. Theoretical results are shown by solid lines, and (b) the corresponding theoretical Fermi surfaces, cited from Refs. [11,12].

$$C_m = \gamma T \tag{2}$$

The electronic specific heat γ can be obtained as follows:

$$\gamma = \frac{R \ln 2}{T_K} \simeq \frac{10^4}{T_K} \left(\mathrm{mJ/K^2\,mol}\right) \tag{3}$$

For example, the γ value and the Kondo temperature T_K in $CeCu_6$ are 1600 mJ/(K^2 mol) and 5 K, respectively. The localized $4f$ electronic state at high temperatures is thus changed into an f-derived band with a flat energy vs momentum dispersion, possessing an extremely large effective mass.

The Doniach phase diagram can be simply understood from the relation between the lattice constant a and the γ value in UX_3 (X: Si, Ge, Sn and Pb) with the $AuCu_3$-type cubic structure, as shown in Fig. 1(c) [5]. USi_3 and UGe_3 are Pauli paramagnets. USn_3 is a spin-fluctuating compound, and UPb_3 is an antiferromagnet. The variety in the magnetic properties is closely related to the lattice constant a, or the distance between the nearest U atoms and to the hybridization of 5f electrons with the other valence electrons. It is stressed that the variety is reflected in the γ value. Namely, the heavy fermion state with large γ value and large cyclotron effective mass m_c^* is formed in the vicinity of the magnetically ordered state. Anisotropic superconductivity is observed in the heavy fermion state. Typical heavy fermion superconductors are UPt_3 [6], $NpPd_5Al_2$ [7], and UGe_2 [8].

In this paper, we present the electronic states of the heavy fermion superconductors UPt_3 and $NpPd_5Al_2$, and of the ferromagnetic pressure-induced superconductor UGe_2, focusing on the Fermi surface and superconducting properties.

2. Heavy fermion spin-triplet superconductor UPt_3

The hexagonal compound UPt_3 exhibits a superconducting ground state characterized by anisotropic spin-triplet pairing [9,10]. Superconductivity in UPt_3 coexists with antiferromagnetic ordering, the Néel temperature being about 5 K. This ordering is, however, not static but dynamical, meaning that antiferromagnetic ordering is not observed in the specific heat and magnetic susceptibility measurements. To understand the nature of the 5f-electrons in UPt_3, it is important to clarify the Fermi surface properties using high-quality single-crystal samples grown by the Czochralski pulling method in a tetra-arc furnace [11,12].

Fig. 2(a) shows the angular dependence of the dHvA frequencies. The origin of the detects ed dHvA branches is identified on the basis of the 5f-itinerant band model. Fig. 2(b) shows the theoretical Fermi surfaces. The dHvA branches are identified as follows: (1) branch ω: band 37-electron, (2) branches τ, σ, ρ, λ, ε, and α: band 36-hole, and (3) branch δ: band 35-hole.

The dHvA frequencies, shown by circles in Fig. 2(a), are in good agreement with theoretical results (solid lines) based on the 5f-itinerant band model. The dHvA branch ω possesses the largest cross-sectional area and cyclotron mass. The cyclotron mass is determined as $80m_0$ in the field range from 150 to 175 kOe for the field along the hexagonal [0001] direction (c-axis), $105m_0$ in the field range from 182 to 196 kOe for [10$\bar{1}$0], and $90m_0$ in the field range of 170 to 196 kOe for [11$\bar{2}$0]. The corresponding band masses are 5.09, 6.84 and 5.79m_0, respectively. The cyclotron masses are about 15 times

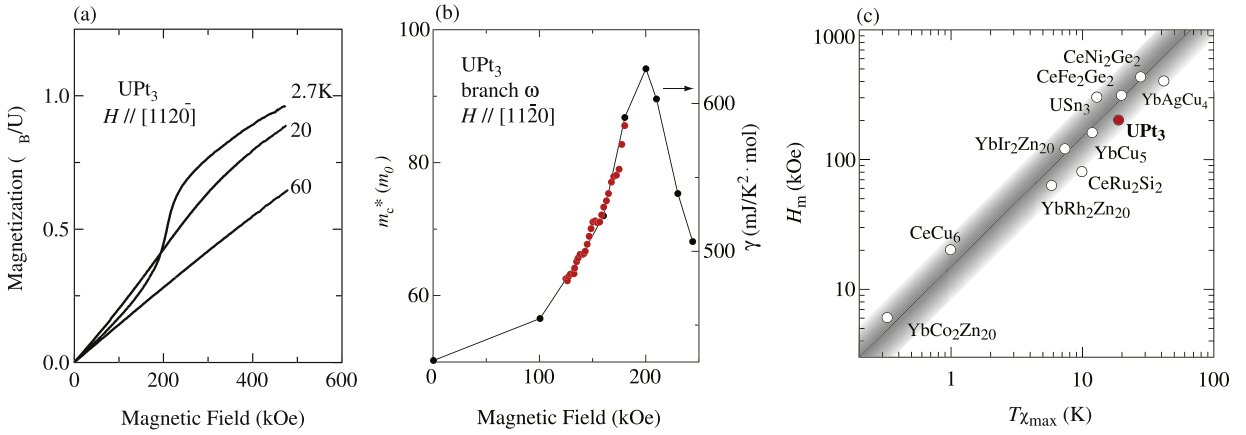

Fig. 3. (Color online.) (a) High-field magnetization, and (b) the field dependencies of the cyclotron mass m_c^* and the γ value in UPt_3, cited from Refs. [13,14]. (c) Relation between $T_{\chi max}$ and H_m in several Ce, Yb, and U compounds including UPt_3. The solid line represents the relation of H_m (kOe) $= 15T_{\chi max}$ (K), cited from Ref. [15].

larger than the corresponding band masses. Note that all the bands contain an f-electron component of about 70% and have flat dispersion.

UPt_3 exhibits a metamagnetic transition at about 200 kOe [13]. Fig. 3(a) shows the high-field magnetization. This metamagnetic transition persists up to about 30 K, which is close to the characteristic temperature $T_{\chi max}$ ($\simeq 20$ K) where the magnetic susceptibility has a maximum in the temperature dependence, as shown in Fig. 1(b). We note the growth of the cyclotron effective mass m_c^* at this metamagnetic transition, as shown in Fig. 3(b). The cyclotron mass in the main band 37-electron Fermi surface, named branch ω, is strongly enhanced with increasing the field from $63m_0$ at 125 kOe to $86m_0$ at 180 kOe [13]. This is consistent with the field dependence of the γ value shown in Fig. 3(b) [14].

It is noted that one of the characteristic properties in the heavy fermion compounds as in UPt_3 is the metamagnetic behavior or an abrupt nonlinear increase of magnetization at the magnetic field H_m below $T_{\chi max}$. Fig. 3(c) shows the relation between $T_{\chi max}$ and H_m in several Ce, Yb, and U compounds including UPt_3 [15]. A solid line represents a relation of H_m (kOe) $= 15T_{\chi max}$ (K), namely $\mu_B H_m = k_B T_{\chi max}$. The γ values or the cyclotron masses m_c^* become maxima at H_m in these compounds [15].

It can be thus concluded that the 5f electrons in UPt_3 are of itinerant nature. Namely, the dHvA results are well explained by the 5f-itinerant band model. All the dHvA branches are heavy, with large cyclotron masses of $15–105m_0$, i.e. ten to twenty times larger than the corresponding band masses. The mass enhancement is caused by magnetic fluctuations, where the freedom of charge transfer of the 5f electrons appears in the form of the 5f-itinerant band, namely the Fermi surface, but the freedom of spin fluctuations of the same 5f electrons reveals an unusual magnetic ordering and enhances the effective mass as in the many-body Kondo effect. These heavy conduction electrons or quasiparticles condense into Cooper pairs. To avoid a large overlap of the wave functions of the paired particles, the heavy fermion state would rather choose an anisotropic channel, like a spin triplet to form Cooper pairs in UPt_3 [6,9,10].

As shown in Fig. 4(a), three superconducting phases named A, B, and C exist in the temperature-field phase diagram [16,17]. The power-law dependence of the thermodynamic and transport quantities suggest two kinds of nodes in the superconducting gap: line and point nodes [10]. Moreover, a spin-triplet (odd-parity) pairing is suggested from the nuclear magnetic resonance study of the Knight shift [9]. One of the most conclusive ways to identify the pairing symmetry is to determine the gap structure by thermal conductivity measurements performed deep inside the superconducting state in presence of a magnetic field assuming different orientations relative to the crystal axes [18].

Fig. 4(b) shows the thermal conductivity $\kappa(\phi)$ normalized by the normal state value κ_n as a function of the azimuthal angle ϕ in the hexagonal basal planes ($\theta = 90°$) at 50 mK under magnetic fields of 30, 10, and 5 kOe. Here, ϕ is measured from the a-axis. In the normal state ($H = 30$ kOe) and the B phase (5 kOe), we find no ϕ dependence. By contrast, what is remarkable is that $\kappa(\phi)$ exhibits a twofold oscillation with a minimum at $\phi = 0°$ ($H \parallel a$-axis), revealing $\kappa(\phi) = \kappa_0 + C_{2\phi}\cos 2\phi$. Note that the twofold symmetry is lower than the sixfold symmetry in the crystal structure, and is inconsistent with the fourfold symmetry expected from one of the previous plausible paring models, E_{2u} [10].

We present furthermore the polar angle θ dependence of $\kappa(\theta)/\kappa_n$ in Fig. 4(c), measured by rotating H within the ac and bc planes at 50 mK under $H = 15, 10,$ and 5 kOe. Here, θ is measured from the c-axis. The dominant twofold oscillation is found in all the fields with maxima at $\theta = 90°$ ($H \parallel a$ and b). In the B phase ($H = 5$ kOe), the two different scanning procedures within the ac and bc planes converge with each other, in a way consistent with the ϕ dependence of κ. In addition, we find extra two minima around $\theta \simeq 20°$ and 160°, shown by arrows. By plotting $\Delta\kappa(\theta)/\kappa_n = (\kappa(\theta) - \kappa_0 - \kappa_{2\theta})/\kappa_n$ vs. θ after the subtraction of a θ-independent term κ_0 and a twofold component $\kappa_{2\theta} = C_{2\theta}\cos 2\theta$ originating from the out-of-plane twofold anisotropy of the Fermi surface and/or magnetothermal resistance, the minima become clearly

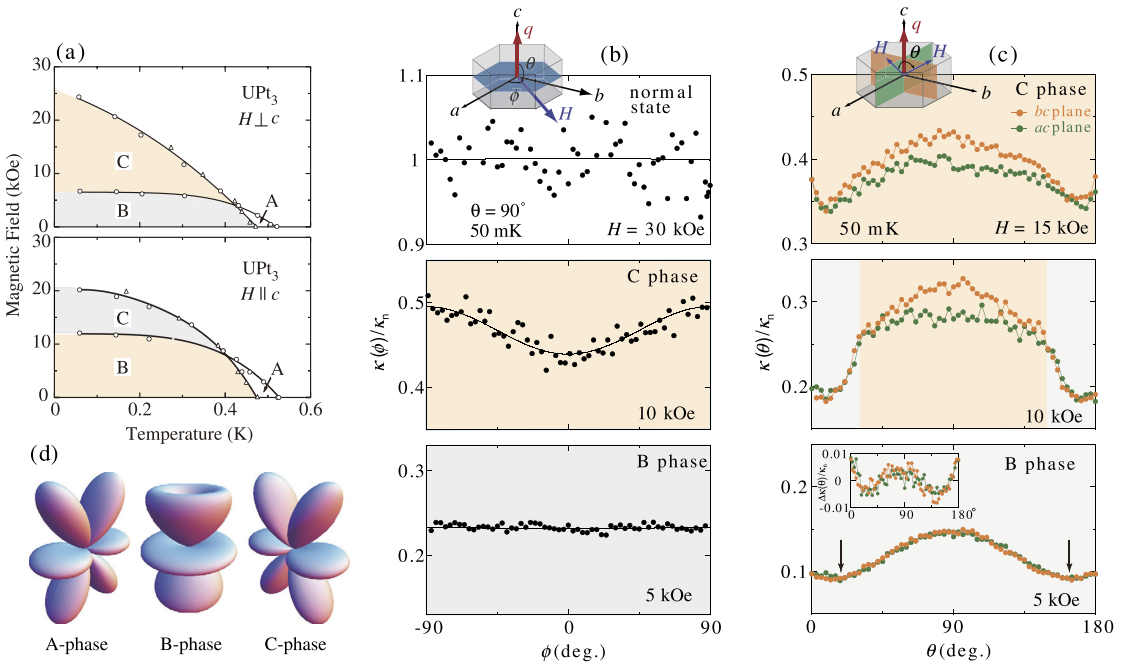

Fig. 4. (Color online.) (a) Phase diagram of UPt_3 with the tree superconducting phases named A, B, and C, (b) and (c) the angular dependencies of the thermal conductivities, and (d) schematic shapes of the gap symmetries in the A, B, and C phases, cited from Refs. [16–18]. Inset in (c) B phase ($H = 5$ kOe) indicates $\Delta\kappa(\theta)/\kappa_n = (\kappa(\theta) - \kappa_0 - \kappa_{2\theta})/\kappa_n$ as a function of θ at 50 mK (see text).

visible around 35° and 145°, as shown in the inset of Fig. 4(c) in the B phase (5 kOe). This double minimum structure is also found in the C phase, revealing that these minima are derived from the two horizontal line nodes at the tropics.

In contrast to the B phase, the two scanning results do not coincide in the C phase. The difference is diminished at $\theta = 0°$ ($H \parallel c$-axis) and maximized at $\theta = 90°$ ($H \parallel a, b$), being consistent with the in-plane two fold symmetry. Moreover, a significant appearance of the twofold symmetry across the BC transition can be seen at 10 kOe, as shown in Fig. 4(c) at 10 kOe. These experimental results are summarized as follows: (1) the line node is along the a-axis in the C phase; (2) the in-phase gap anisotropy is absent in the B phase; and (3) the two horizontal line nodes are at the tropics in both B and C phases. Taking into account all these results and the ***d***-vector configurations assigned by the Knight shift, the pairing symmetry is concluded to be $\mathbf{b}k_a(5k_c^2 - 1)$ in the A phase, $(\mathbf{b}k_a + \mathbf{c}k_b)(5k_c^2 - 1)$ in the B phase, and $\mathbf{c}k_b(5k_c^2 - 1)$ ($\mathbf{H} \parallel \mathbf{ab}$), or $\mathbf{a}k_b(5k_c^2 - 1)$ ($\mathbf{H} \parallel \mathbf{c}$) in the C phase, where **a**, **b**, and **c** are unit vectors of the hexagonal axes representing the directions of ***d*** vectors. The pairing symmetry of UPt_3 is determined to be an E_{1u} representation in the f-wave category, and the spin part of the pair function is most likely of weak spin-orbit coupling, where the corresponding ***d***-vector can change its orientation against the magnetic field.

3. Heavy fermion superconductor $NpPd_5Al_2$

$NpPd_5Al_2$ crystallizes in the tetragonal structure ($I4/mmm$), which is similar to the tetragonal structure ($P4/mmm$) of $CeCoIn_5$ and $PuCoGa_5$, as shown in Fig. 5 [7,16]. The $5s^25p^1$ ($4s^24p^1$) electrons of the In(Ga) atoms in $CeCoIn_5$ ($PuCoGa_5$) are, however, replaced by the 4d electrons of the Pd atom in $NpPd_5Al_2$. The 4d electrons in $NpPd_5Al_2$ are well hybridized with the 5f electrons, and produce strongly correlated conduction electrons. We grew single crystals of $NpPd_5Al_2$ by the Pb-flux method.

$NpPd_5Al_2$ does not order magnetically. The corresponding magnetic susceptibility increases steeply with decreasing temperature, but a sudden drop of the susceptibility occurs below $T_{sc} = 4.9$ K due to the onset of superconductivity, as shown in Fig. 6(a). This is very similar to what observed in $CeCoIn_5$, as shown in Fig. 6(c) [19,20], but is unusual because the magnetic susceptibility of the heavy fermion compound UPt_3, mentioned above, has a maximum at $T_{\chi\,max} \simeq 20$ K, and becomes constant at lower temperatures. This is due to the fact that (as in $CeCoIn_5$) the electronic ground state of $NpPd_5Al_2$ is located in the vicinity of an antiferromagnetically ordered state, namely, in the QCP region. In fact, the low-temperature electrical resistivity of $NpPd_5Al_2$ does not follow the Fermi liquid relation $\rho = \rho_0 + AT^2$, but indicates a T-linear dependence. The γ value is large, $\gamma = 200$ mJ/(K^2 mol) at $T_{sc} = 4.9$ K, and is enhanced to be 390 mJ/(K^2 mol) at 0 K from the entropy balance. The large paramagnetic effect is reflected in the strong suppression of the upper critical field H_{c2}, as shown in Fig. 6(e), and correspondingly, a step-like increase of the magnetization is observed at H_{c2}, as shown in Fig. 7(a).

In the case of the typical d-wave ($d_{x^2-y^2}$) superconductor $CeCoIn_5$, a large paramagnetic effect induces a first-order phase transition at H_{c2}, namely, the step-like increase of the magnetization, at temperatures lower than $0.3T_{sc}$ or $0.4T_{sc}$

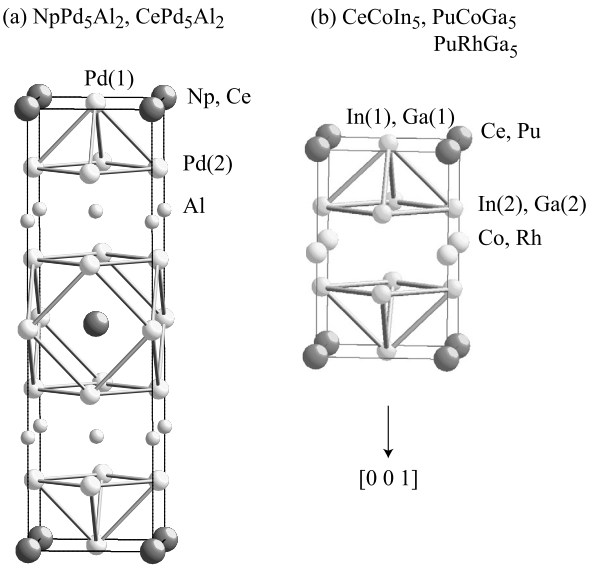

Fig. 5. Tetragonal crystal structures of (a) $NpPd_5Al_2$ and $CePd_5Al_2$, and (b) $CeCoIn_5$, $PuCoGa_5$, and $PuRhGa_5$, cited from Ref. [16].

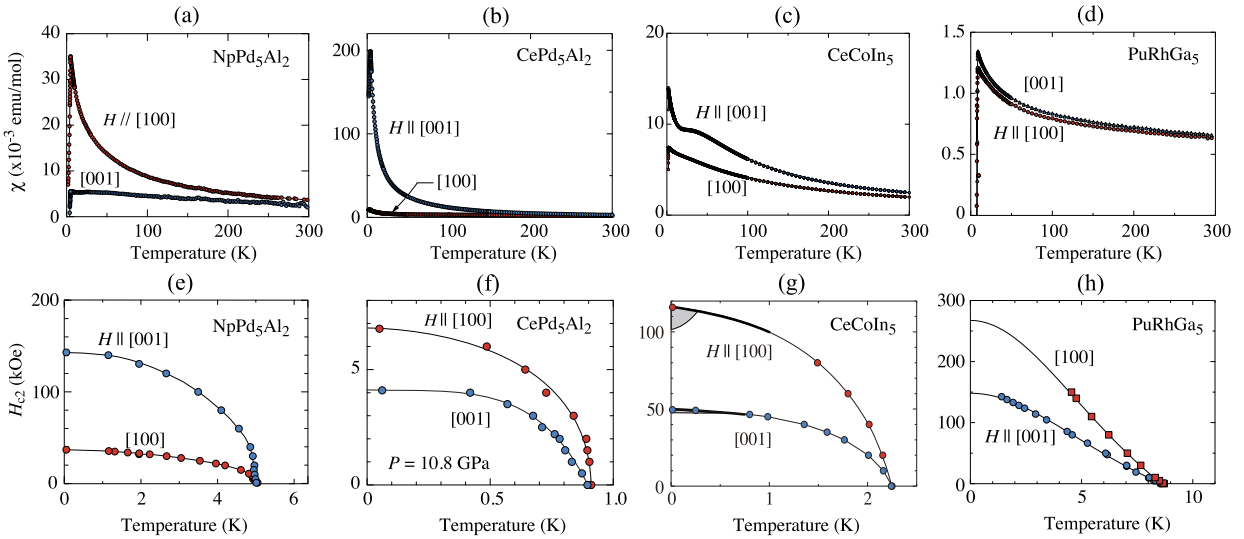

Fig. 6. (Color online.) Temperature dependencies of the magnetic susceptibility χ and the upper critical field H_{c2} in $NpPd_5Al_2$ (a, e) [7], $CePd_5Al_2$ (b, f) [24], $CeCoIn_5$ (c, g) [19,20], and $PuRhGa_5$ (d, h) [25], respectively.

($T_{sc} = 2.3$ K), as shown in Fig. 7(b) [21]. A similar phenomenon is realized in $NpPd_5Al_2$. Surprisingly, the step-like increase of magnetization is observed up to a higher temperature of 3 K ($= 0.6T_{sc}$). Note that thick lines in Fig. 6(g) correspond to the first-order phase transition. The shaded region in the superconducting mixed state just below H_{c2} is discussed from the viewpoint of the Fulde–Ferrell–Larkin–Ovchinikov state for $CeCoIn_5$ [20].

The γ value of 1070 mJ/(K^2 mol) at $H_{c2} \simeq 50$ kOe for $H \parallel [001]$ in $CeCoIn_5$ is strongly reduced with increasing magnetic field. The corresponding cyclotron effective mass of $86m_0$ at 100 kOe is reduced to $47m_0$ at 160 kOe [19]. To confirm the reduction of the γ value in $NpPd_5Al_2$, we measured the field dependence of the A value in the Fermi-liquid relation of the electrical resistivity $\rho = \rho_0 + AT^2$ at magnetic fields larger than $H_{c2} = 37$ kOe for $H \parallel [100]$. This is because the temperature dependence of the electrical resistivity under magnetic fields lower than 50 kOe does not follow the T^2-dependence, revealing the non-Fermi liquid character. As shown in Fig. 7(c), the A value is strongly reduced by the application of a magnetic field [22]. Correspondingly, the γ value should be reduced with increasing the magnetic field because of the Fermi liquid relation $\gamma \sim \sqrt{A}$.

In order to further clarify the stability of the superconducting state at high pressure, we measured the pressure dependence of T_{sc}, as shown in Fig. 7(d). $T_{sc} \simeq 5$ K at ambient pressure is reduced to zero at 5.7 GPa [22].

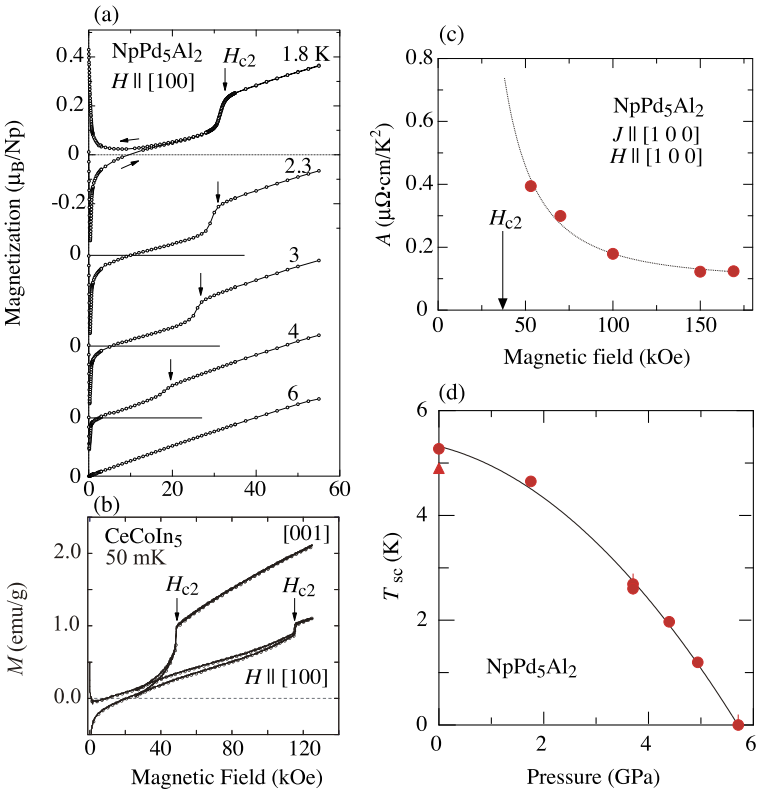

Fig. 7. (Color online.) Magnetization curves of (a) $NpPd_5Al_2$ [7] and (b) $CeCoIn_5$ [21], revealing a step-like increase of the magnetization at H_{c2}, cited from Refs. [7,21]. (c) Field dependence of the A value for $H \parallel [100]$ in $NpPd_5Al_2$, and (d) pressure dependence of T_{sc}, cited from Ref. [22].

It is noticed that the normal and superconducting properties of $NpPd_5Al_2$ are very similar to those of $CeCoIn_5$, but the anisotropy of the magnetic susceptibility and the upper critical field are different in the two compounds. If we simply analyze the anisotropy of the upper critical field from the so-called effective mass model, we deduce that the Fermi surface in $NpPd_5Al_2$ has a pan-cake shape. The corresponding Fermi surface based on the 5f-itinerant band model is, however, quasi-two dimensional, as shown in Fig. 8(a) [23].

In Figs. 6 and 8, we present the magnetic susceptibility, upper critical field, and theoretical Fermi surface in $CePd_5Al_2$ [24], $CeCoIn_5$ [19,20], and $PuRhGa_5$ [25] ($PuCoGa_5$ [26]) for comparison. $CePd_5Al_2$ is an antiferromagnet $T_N = 4.1$ K at ambient pressure, but becomes superconductive in the pressure range from 9 to 12 GPa [27]. The 4f electrons of $CePd_5Al_2$ at 10.8 GPa become itinerant because the Néel temperature becomes zero and the system enters the paramagnetic state. The magnetic susceptibility at ambient pressure in Fig. 6(b) is well explained by the CEF scheme with the magnetic easy-axis along the tetragonal [001] direction in $CePd_5Al_2$ [24], in contrast with the [100] easy-axis in $NpPd_5Al_2$.

On the other hand, the anisotropy of the upper critical field in $PuRhGa_5$ without magnetic ordering, shown in Fig. 6(h), is understood by the quasi-two-dimensional Fermi surfaces of the similar compound $PuCoGa_5$ shown in Fig. 8(d) [25,26]. One of the characteristic properties in $NpPd_5Al_2$ and in its related compounds is the quasi-two dimensionality of the electronic state, represented by nearly-cylindrical Fermi surfaces along the tetragonal [001] direction. Furthermore, the quasi-two dimensional electronic state, together with the heavy fermion state, enhances the heavy fermion superconductivity. In fact, the superconducting transition temperature $T_{sc} = 0.2$ K in the three-dimensional electronic state of $CeIn_3$ under 2.6 GPa is enhanced to $T_{sc} = 2.3$ K in $CeCoIn_5$ [19]. Interesting is a relation between the superconducting transition temperature T_{sc} and the γ value, as shown in Fig. 9: $T_{sc} = 2.3$ K and $\gamma = 380$ mJ/(K^2 mol) in $CeCoIn_5$ [28], 4.9 K and 200 mJ/(K^2 mol) in $NpPd_5Al_2$ [7], and 18.5 K and 100 mJ/(K^2 mol) in $PuCoGa_5$ [29], as shown in Fig. 9. Note that the γ value in $CeCoIn_5$ is 380 mJ/(K^2 mol) at $T_{sc} = 2.3$ K and is enhanced to 1070 mJ/(K^2 mol) at 0.2 K. The γ value in $CeIn_3$ under 2.6 GPa is roughly estimated as 1000 mJ/(K^2 mol) from the cyclotron mass close to $100m_0$ [30].

4. UGe_2

UGe_2 crystallizes in the orthorhombic crystal structure ($Cmmm$, $a = 4.0089$ Å, $b = 15.0889$ Å, and $c = 4.0950$ Å) with a large lattice constant along the b-axis, as shown in Fig. 10(a), which corresponds to a short distance along the b-axis in the Brillouin zone [31]. A U zigzag chain with next-nearest-neighbor distance $d_{U-U} = 3.85$ Å is formed along the a-axis.

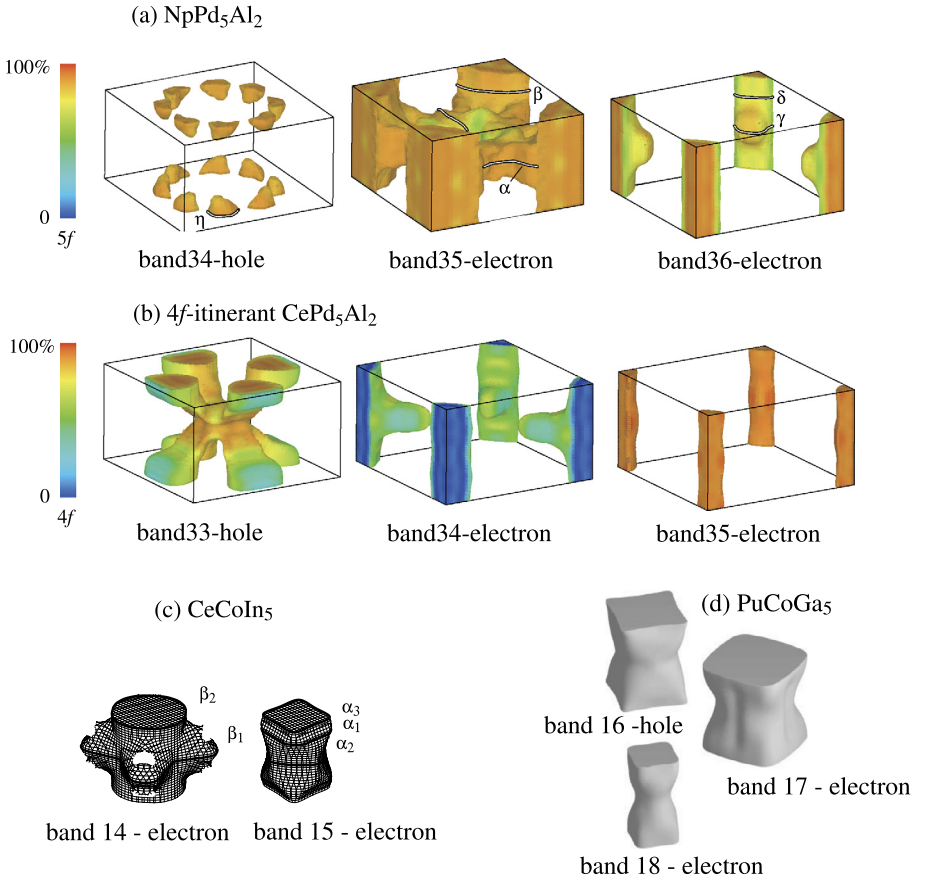

Fig. 8. (Color online.) Theoretical Fermi surfaces based on the f-itinerant band model in (a) $NpPd_5Al_2$ [23], (b) $CePd_5Al_2$ [24], (c) $CeCoIn_5$ [19], and (d) $PuCoGa_5$ [26].

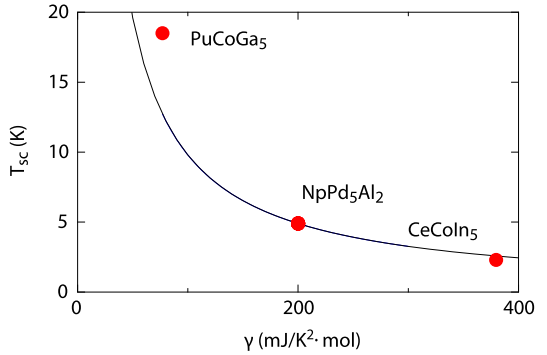

Fig. 9. (Color online.) Relation between the superconducting transition temperature T_{sc} and the electronic specific heat coefficient γ in quasi-two-dimensional superconductors $CeCoIn_5$ [28], $NpPd_5Al_2$ [7], and $PuCoGa_5$ [29]. Note that the γ value of $CeCoIn_5$ is 380 mJ/(K^2 mol) at $T_{sc} = 2.3$ K and is enhanced to 1070 mJ/(K^2 mol) at 0.2 K.

The ordered moment of $\mu_s \simeq 1.4\mu_B$/U is oriented along the *a*-axis, being the magnetic easy-axis, whilst the *b*- and *c*-axes correspond to hard axes in the magnetization curves. UGe_2 is thus an Ising-type ferromagnet.

UGe_2 is a characteristic pressure-induced superconductor in the ferromagnetic state, suggesting the so-called equal spin pairs of ↑↑ or ↓↓ [8,32]. The coexistence of ferromagnetism and superconductivity is realized in this compound, together with the similar compounds URhGe, UCoGe, and most likely UIr. Up to date, this is limited only in 5f-itinerant ferromagnets. In the pressure experiment of UGe_2 in Fig. 10(b) [33], it was found that the Curie temperature $T_C = 52$ K becomes zero at $P_c \simeq 1.5$ GPa. A second phase transition was found at $T^* \simeq 30$ K at ambient pressure, and becomes zero at $P_c^* \simeq 1.2$ GPa. The temperature region from T_C to T^* and/or the pressure region from P_c^* to P_c are/is named the weakly polarized phase (FM1) with ordered moments of about $0.9\mu_B$/U, as shown later in Fig. 11(a), whilst the lower-temperature region

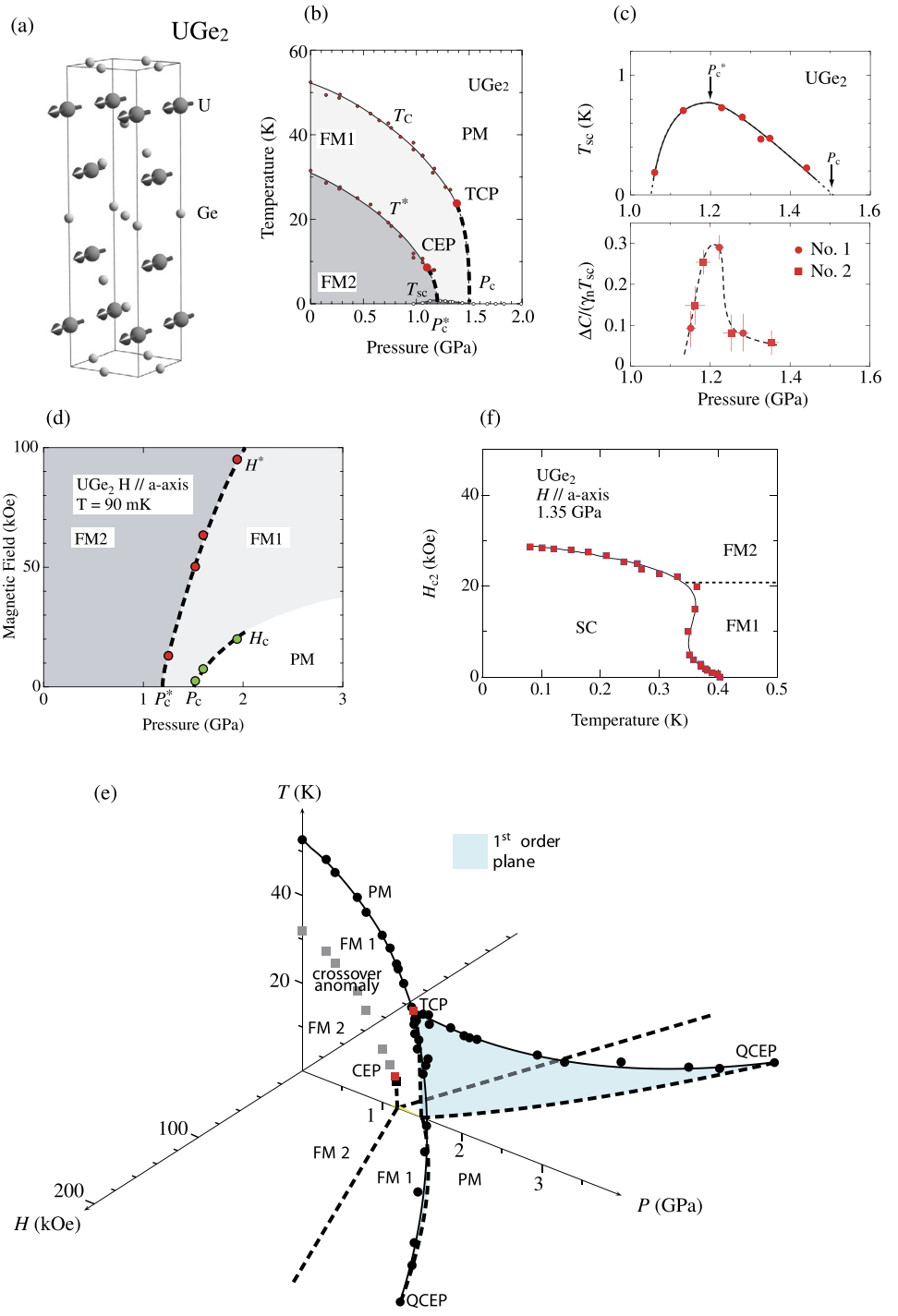

Fig. 10. (Color online.) (a) Orthorhombic crystal structure in UGe_2 [31]. Arrows on the U sites denote the direction of the magnetic moment. (b) Temperature vs pressure phase diagram [33]. (c) Pressure dependencies of T_{sc} determined by the resistivity measurement (upper panel) and the specific heat jump of $\Delta C/\gamma_n T_{sc}$ (lower panel) [38]. (d) Pressure dependence of the magnetic phase transition fields [36]. (e) Temperature–pressure–field phase diagram for $H \parallel a$-axis, and (f) temperature dependence of H_{c2} for $H \parallel a$-axis at 1.35 GPa, cited from Refs. [32,37]. TCP, CEP, and QCEP are the tricritical point, critical end point, and quantum critical end point, respectively.

($T < T^*$) and/or the pressure region below P_c^* are/is named the strongly polarized phase (FM2), with ordered moments of 1.41–1.26μ_B/U [34,35]. Note that the phase transition at T^* is understood as a cross-over anomaly at ambient pressure because the magnetic moment increases smoothly between FM1 and FM2 and there exist no changes of the crystal structure and magnetic structure. On the other hand, a step-like change of the magnetic moment is observed between FM1 and FM2

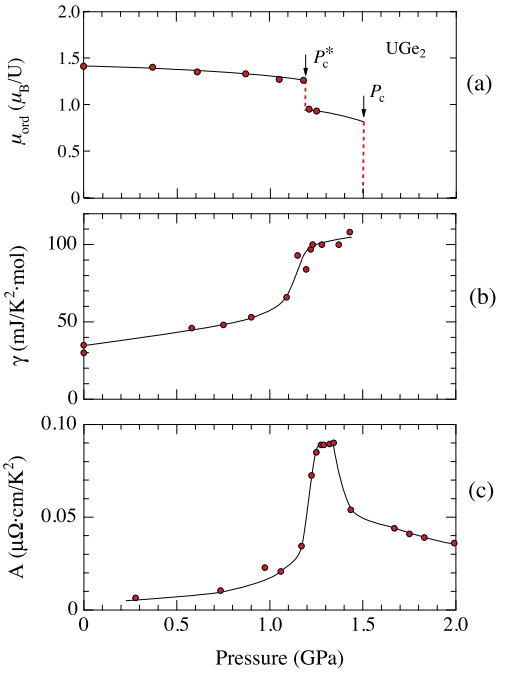

Fig. 11. (Color online.) Pressure dependencies of (a) ordered moment μ_{ord}, (b) electronic specific heat γ, and (c) A-value in UGe_2, cited from Refs. [33] and [34].

with increasing pressure. Two solid lines showing T_C and T^*, namely, a T_C line in the pressure region from a pressure corresponding to a tricritical point (TCP) to P_c, and a T^* line in the pressure region from a pressure corresponding to a critical end point (CEP) to P_c^* are of the first order [32] (shown by thick broken lines in Fig. 10(b)).

When the magnetic field is applied along the a-axis, the FM1 phase is changed into the FM2 phase at H^* in the pressure region from P_c^* to P_c, as shown in Fig. 10(d), and even in the pressure region of $P > P_c$, revealing a phase change from the paramagnetic (PM) phase to the FM1 phase at H_c. This corresponds to the metamagnetic transition, indicating a step-like increase of magnetization. The P–H phase diagram at 90 mK is shown in Fig. 10(d) [36]. Note that two lines showing H^* and H_c, shown by thick broken lines connecting the data, are of the first order. The P–H–T phase diagram is also shown in Fig. 10(e) [32,37].

Superconductivity appears in the ferromagnetic state. Fig. 10(c) shows the pressure dependence of T_{sc} obtained by electrical resistivity measurements and the pressure dependence of $\Delta C/\gamma_n T_{sc}$ (ΔC: jump of the specific heat at T_{sc}, γ_n: electronic specific heat coefficient at T_{sc}) obtained by specific heat measurements [38]. The superconducting region is wide in the resistivity measurement (upper figure) compared with that in the specific heat measurement (lower figure), but T_{sc} indicates a maximum at $P_c^* \simeq 1.2$ GPa. The specific heat jump $\Delta C/\gamma_n T_{sc}$ is much smaller than 1.43 in the weak coupling BCS scheme. Note that the residual specific heat coefficient estimated at 0 K is quite large, 70% of the γ value in the normal state, in spite of a very high-quality single-crystal sample with the residual resistivity ratio (ρ_{RT}/ρ_0, ρ_{RT}: resistivity at room temperature, ρ_0: residual resistivity) RRR = 600 and $\rho_0 = 0.2$ μΩ cm, which was obtained by the Czochralski method. This might be related to a large magnetic moment of about $0.9\mu_B$/U, shown in Fig. 11(a), and the corresponding self-induced vortex state. Note that the residual specific heat coefficient and the ordered moment are 50% and $0.4\mu_B$/U in URhGe, and 15% and $0.05\mu_B$/U in UCoGe [32]. A relation between the residual specific heat coefficient and the magnetic moment has been recently discussed theoretically [39].

A striking point on the superconducting properties is that the temperature dependence of H_{c2} for $H \parallel a$-axis indicates the field-enhanced superconducting phase when the pressure is tuned just above P_c^*, as shown in Fig. 10(f) [32,37]. This peculiar "S"-shape of the H_{c2} curve under $P = 1.35$ GPa is associated with the crossing of the metamagnetic transition at H^*, namely a change of the magnetic phase from FM1 to FM2.

As shown in Fig. 11(b) and 11(c), which was obtained from the resistivity and specific heat experiments, the A value of the electrical resistivity ρ ($= \rho_0 + AT^2$) displays a peak at about 1.3 GPa. The corresponding electronic specific heat coefficient γ reaches 100 mJ/(K^2 mol). The main Fermi surfaces, which were determined by dHvA experiments and energy band calculations, are nearly cylindrical along the b-axis [40–42]. The corresponding cyclotron masses are relatively large, being 15–20m_0. It was concluded that 5f-electrons in UGe_2 are itinerant, indicating band magnetism as in 3d-electron systems.

To further clarify the Fermi surface property, we carried out the dHvA experiment under pressure. We found a drastic change of the Fermi surfaces when the pressure crosses p_c [33].

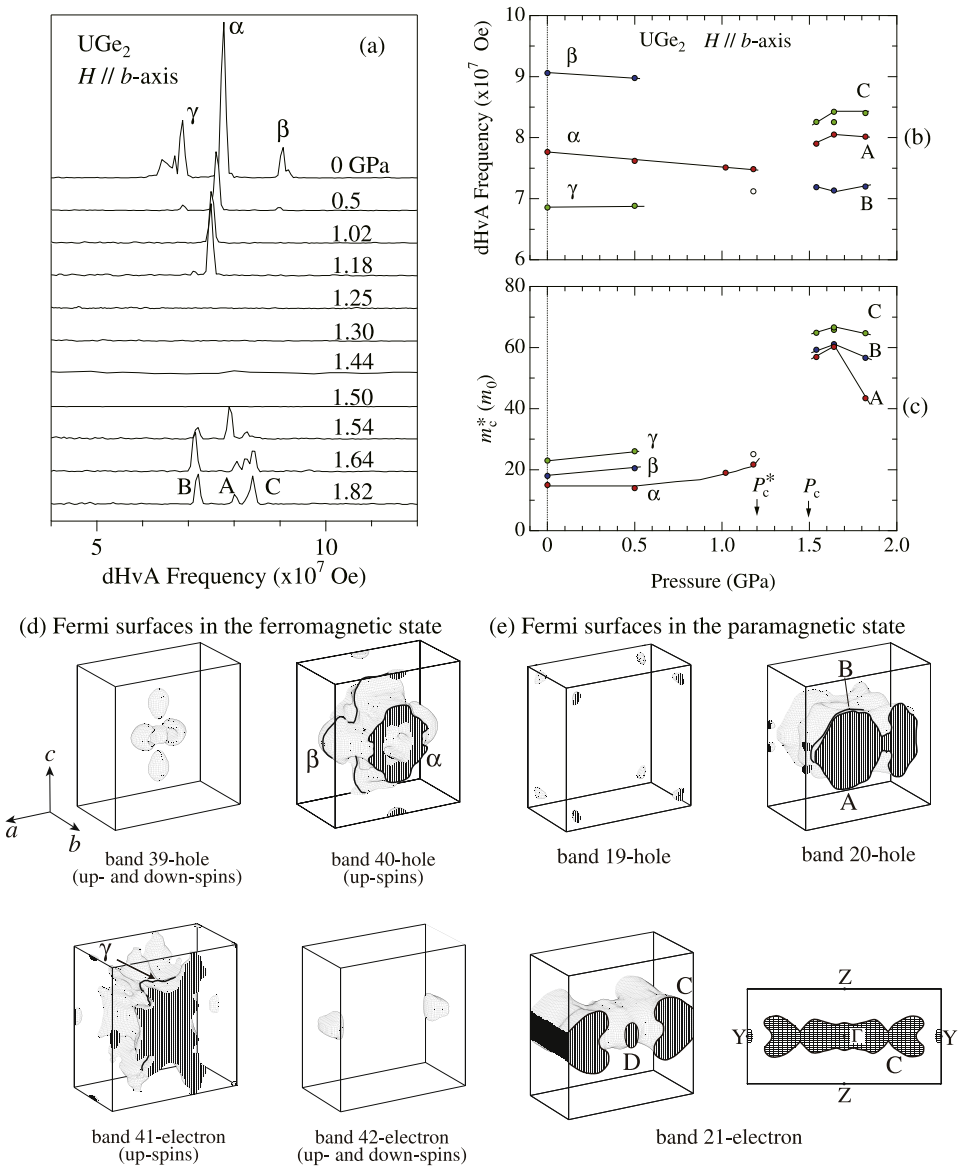

Fig. 12. (Color online.) (a) FFT spectra under various pressures for the magnetic field along the *b*-axis (hard-axis), pressure dependencies of (b) the dHvA frequencies and (c) the cyclotron masses, and theoretical Fermi surfaces in (d) the ferromagnetic (FM2 phase) and (e) paramagnetic states in UGe_2, cited from Ref. [33].

Fig. 12 shows the FFT spectra at several pressures. The FFT spectra are highly different below and above about 1.5 GPa ($= P_c$). In the present dHvA experiment, we obtained no dHvA signal in the pressure region from 1.25 to 1.50 GPa, namely, in the FM1 phase, but a clear signal was observed at 1.54 GPa.

We show in Figs. 12(b) and 12(c) the pressure dependencies of the dHvA frequencies and the cyclotron effective masses. The dHvA frequency of branch α, together with that of branch β, decreases almost linearly with increasing pressure, as shown in Fig. 12(b). The cyclotron mass of $15m_0$ for branch α at ambient pressure increases up to $22m_0$ at 1.18 GPa with a tendency to a steep increase above $p_c^* \simeq 1.2$ GPa, as shown in Fig. 12(c). The cyclotron masses in the paramagnetic state are surprisingly large: 43, 57, 64 and $19m_0$ at 1.82 GPa for branches A, B, C and D, respectively. Note that branch D is not shown in Figs. 12(b) and 12(c) because of a small dHvA frequency $F = 1.59 \times 10^7$ Oe. The cyclotron masses in the paramagnetic state have a decreasing tendency with increasing pressure, which is approximately consistent with the A value in Fig. 11(c). It is noted that similar dHvA results are obtained [43,44].

We will discuss a change of the Fermi surface under pressure under consideration of the theoretical results of energy band calculations in the ferromagnetic (FM2 phase) and paramagnetic states shown in Figs. 12(d) and 12(e), respectively. Fermi surfaces were calculated in the scheme of a fully-relativistic spin-polarized version of the linearized augmented-plane-wave (LAPW) method within a local spin-density approximation under the assumption that 5f electrons are itinerant and

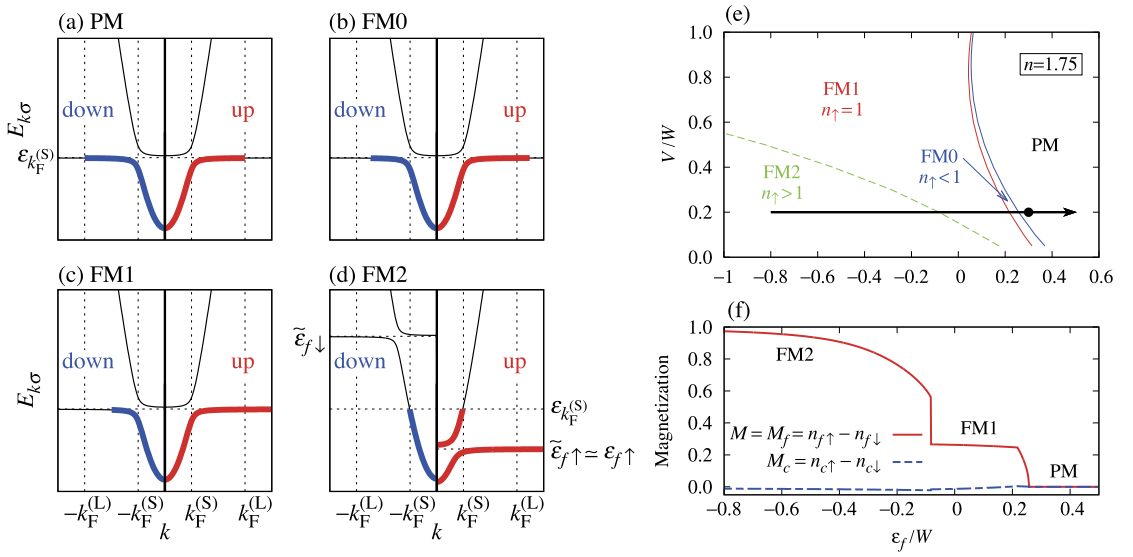

Fig. 13. (Color online.) Schematic band structures of paramagnetic and ferromagnetic phases in the periodic Anderson model. (a) Paramagnetic phase (PM), (b) weakly polarized ferromagnetic phase (FM0), (c) half-metallic phase (FM1), and (d) ferromagnetic phase with an almost completely polarized f-electron state (FM2), cited from Ref. [45]. $E_{k\sigma}$ denotes the quasiparticle energy. The right-hand (left-) part of each figure shows the up- (down-) spin band. The occupied states are represented by the bold lines. (e) Theoretical phase diagrams for the total number $n = n_\uparrow + n_\downarrow$ of electrons per site, $n = 1.75$. Solid lines indicate the second-order phase transitions, and a dashed line indicates the first-order phase transition. A bold arrow indicates the parameter set for which the magnetization was calculated in (f).

the magnetic moment is directed along the a-axis in the ferromagnetic state. Band 40-hole and 41-electron Fermi surfaces in Fig. 12(d) correspond to majority up-spin bands, while minority down-spin states are included partially in band 39-hole and 42-electron Fermi surfaces. In the present band calculations, a magnetic moment of $1.2\mu_B$/U was obtained, where spin and orbital moments are $-1.3\mu_B$/U and $2.5\mu_B$/U, respectively.

The characteristic pressure range is classified into three regions, as presented above: (1) $p < p_c^*$, (2) $p_c^* < p < p_c$ and (3) $p > p_c$. In the first pressure region where $p < p_c^*$, the dHvA frequency of branch α, which most likely corresponds to the majority up-spin band 40-hole Fermi surface, decreases almost linearly with increasing pressure. This means that the volume of the majority up-spin band 40-hole Fermi surface decreases with increasing pressure. Correspondingly, the Curie temperature T_C decreases from 52 K at ambient pressure to about 30 K at p_c^*, and an ordered moment decreases from 1.41 to about $1.26\mu_B$/U. Simply thinking, it is expected that with increasing pressure, volumes of both the band 40-hole and the band 41-electron Fermi surfaces with majority up-spin states decrease, while volumes of both the band 39-hole and the band 42-electron Fermi surfaces with minority down-spin states increase correspondingly. Note that both the up- and down-spin states are involved in the band 39-hole and band 42-electron Fermi surfaces at ambient pressure. The ordered moment, which is proportional to the volume difference between up- and down-spin states, thus decreases with increasing pressure. Experimentally, however, we have found no direct evidence for the Fermi surface with down-spin state. The dHvA frequency of 7.12×10^7 Oe was observed at 1.18 GPa. It is not clear whether this branch corresponds to the Fermi surface with minority down-spin states or not.

Next we will discuss the electronic state in the second pressure region where $p_c^* < p < p_c$. In this pressure region, the dHvA signal disappears completely. There are few reasons for this. One is a large γ value in this region. The γ value reaches 100 mJ/(K^2 mol), as shown in Fig. 11(b), which is extremely larger than 35 mJ/(K^2 mol) at ambient pressure. A large effective mass of the conduction electron reduces intensively the dHvA amplitude.

In the paramagnetic state we observed clear dHvA oscillations. Branches A, B, C and D are approximately identified in theoretical Fermi surfaces in Fig. 12(e), which were calculated by using the lattice parameter at ambient pressure in the paramagnetic state. As shown in Fig. 12(e), UGe_2 is a compensated metal because it possesses two molecules in the primitive cell. Band 19- and 20-hole Fermi surfaces are compensated by a band 21-electron Fermi surface, and up- and down-spin states are degenerate in the paramagnetic state. Four kinds of theoretical dHvA frequencies corresponding to branches A, B, C and D are: 9.21×10^7 Oe ($8.74m_0$), 5.00×10^7 Oe ($12.2m_0$), 11.7×10^7 Oe ($14.2m_0$) and 0.38×10^7 Oe ($6.01m_0$), respectively. These dHvA frequencies are quantitatively not in good agreement with the experimental values, although a rough correspondence between the theory and the experiment is obtained. This discrepancy is mainly due to the low symmetry of the orthorhombic crystal structure.

The electronic states at low temperatures are thus changed as a function of pressure, from the strongly polarized ferromagnetic state (FM2) to the weakly polarized one (FM1), and finally to the paramagnetic state (PM). We will furthermore introduce one of the theoretical discussions on these phase changes as well the ordered moments and the effective masses [45].

The theory is based on the periodic Anderson model. The theoretical results are simply shown in Fig. 13. In the paramagnetic phase shown in Fig. 13(a), the numbers of up- and down-spin electrons are the same. A large Fermi surface is realized with a Fermi momentum $k_F^{(L)}$ because the f-electron state contributes to the band. With a weak polarization, the band will be changed into a FM0 phase in Fig. 13(b). When the polarization becomes larger, the lower hybridized band will be filled up by the up-spin electrons as shown in Fig. 13(c). This state might be correspond to FM1. In this state, the Fermi surface for the up-spin states disappears, revealing a half-metallic state. When polarization increases furthermore, the up-spin electrons start to fill the upper hybridized band as shown in Fig. 13(d), which might correspond to FM2. In the FM2 state, the f electrons will polarize almost completely. The corresponding electronic state is the small Fermi surface state with a momentum $k_F^{(S)}$. When the f-electron level ϵ_f is shifted upward from the FM2 state, the electronic states are changed into FM2 $\rightarrow$ FM1 $\rightarrow$ FM0 $\rightarrow$ PM, as shown in Fig. 13(e). The corresponding magnetization or the ordered moment $\mu_{\rm ord} = n_{f\uparrow} - n_{f\downarrow}$ is changed as shown in Fig. 13(f). Here, V is the hybridization matrix element, and W is the band width. The effective mass was also calculated (not shown here), revealing a large mass in FM1.

5. Conclusion

We have presented the Fermi surface, magnetic and superconducting properties in UPt_3, $NpPd_5Al_2$, and UGe_2, together with their related compounds. Fascinating anisotropic superconductivity, magnetism, and heavy fermions are observed in these compounds. These are summarized as follows.

1) The 5f-itinerant band model is applicable to the topology of the Fermi surface in a heavy fermion superconductor UPt_3. The detected cyclotron masses are extremely large, reaching $110m_0$. UPt_3 possesses three superconducting phases in the magnetic field–temperature space, named A, B, and C phases. From precise field-angle-resolved thermal conductivity measurements, the pairing symmetry of UPt_3 is found to belong to an E_{1u} representation in the f-wave category.

2) A heavy fermion superconductor $NpPd_5Al_2$ is found to reside in the vicinity of a quantum critical point, similar to the quasi-two dimensional heavy fermion superconductor $CeCoIn_5$ with the $d_{x^2-y^2}$-type symmetry. Therefore, the heavy-fermion superconductivity is realized in the non-Fermi liquid state.

3) UGe_2 is a 5f-itinerant Ising-type ferromagnet, but becomes superconductive in a narrow pressure region of $P_c^* \simeq 1.2$ GPa, most likely in the equal spin pairs of $\uparrow\uparrow$ or $\downarrow\downarrow$. In the temperature–pressure phase diagram, the strongly polarized ferromagnetic (FM2) phase is changed into the weakly polarized ferromagnetic (FM1) phase at $P_c^* \simeq 1.2$ GPa, and furthermore changed into the paramagnetic phase at $P_c = 1.5$ GPa with increasing pressure. The heavy-fermion state, together with anisotropic superconductivity, is realized at around $P_c^* \simeq 1.2$ GPa. According to a recent theory, the FM2 phase has almost completely polarized 5f-electrons, whilst the FM1 phase is half-metallic without the Fermi surface for the majority spin, suggesting that these phase transitions correspond to a change of the topology of the Fermi surface.

Acknowledgements

We are very grateful to N. Kimura, E. Yamamoto, N. Tateiwa, T.C. Kobayashi, H. Harima, and H. Yamagami for their collaboration.

References

[1] Y. Ōnuki, T. Goto, T. Kasuya, in: K.H.J. Buschow (Ed.), Materials Science and Technology, vol. 3A, VCH, Weinheim, Germany, 1991, p. 545, Part I, Ch. 7.
[2] Y. Ōnuki, A. Hasegawa, in: K.A. Gschneidner Jr., L. Eyring (Eds.), Handbook on the Physics and Chemistry of Rare Earths, vol. 20, Elsevier Science, Amsterdam, 1995, p. 1.
[3] Y. Ōnuki, R. Settai, J. Low Temp. Phys. 38 (2012) 89.
[4] S. Doniach, in: R.D. Parks (Ed.), Valence Instabilities and Related Narrow Band Phenomena, Plenum, New York, 1977, p. 169.
[5] Y. Ōnuki, R. Settai, K. Sugiyama, T. Takeuchi, T.C. Kobayashi, Y. Haga, E. Yamamoto, J. Phys. Soc. Jpn. 73 (2004) 769.
[6] G.R. Stewart, Z. Fisk, J.O. Willis, J.L. Smith, Phys. Rev. Lett. 52 (1984) 679.
[7] D. Aoki, Y. Haga, T.D. Matsuda, N. Tateiwa, S. Ikeda, Y. Homma, H. Sakai, Y. Shiokawa, E. Yamamoto, A. Nakamura, R. Settai, Y. Ōnuki, J. Phys. Soc. Jpn. 76 (2007) 063701.
[8] S.S. Saxena, P. Agarwal, K. Ahilan, F.M. Grosche, R.K.W. Haselwimmer, M.J. Steiner, E. Pugh, I.R. Walker, S.R. Julian, P. Monthoux, G.G. Lonzarich, A. Huxley, I. Sheikin, D. Braithwaite, J. Flouquet, Nature 406 (2000) 587.
[9] H. Tou, Y. Kitaoka, K. Ishida, K. Asayama, N. Kimura, Y. Ōnuki, E. Yamamoto, Y. Haga, K. Maezawa, Phys. Rev. Lett. 80 (1998) 3129.
[10] R. Joyint, L. Taillefer, Rev. Mod. Phys. 74 (2002) 235.
[11] N. Kimura, T. Komatsubara, D. Aoki, Y. Ōnuki, Y. Haga, E. Yamamoto, H. Aoki, H. Harima, J. Phys. Soc. Jpn. 67 (1998) 2185.
[12] N. Kimura, T. Tani, H. Aoki, T. Komatsubara, S. Uji, D. Aoki, Y. Inada, Y. Ōnuki, Y. Haga, E. Yamamoto, H. Harima, Physica B 281–282 (2000) 710.
[13] K. Sugiyama, M. Nakashima, D. Aoki, K. Kindo, N. Kimura, H. Aoki, T. Komatsubara, S. Uji, Y. Haga, E. Yamamoto, H. Harima, Y. Ōnuki, Phys. Rev. B 60 (1999) 9248.
[14] H.P. van der Meulen, Z. Tarnawski, A. de Visser, J.J.M. Franse, J.A.A.J. Perenboom, D. Althof, H. van Kempen, Phys. Rev. B 41 (1990) 9352.
[15] Y. Ōnuki, R. Settai, T. Takeuchi, K. Sugiyama, F. Honda, Y. Haga, E. Yamamoto, T.D. Matsuda, N. Tateiwa, D. Aoki, I. Sheikin, H. Harima, H. Yamagami, J. Phys. Soc. Jpn. 81 (2012) SB001.
[16] Y. Haga, H. Sakai, S. Kambe, J. Phys. Soc. Jpn. 76 (2007) 051012.
[17] T. Sakakibara, K. Tenya, M. Ikeda, T. Tayama, H. Amitsuka, E. Yamamoto, K. Maezawa, N. Kimura, R. Settai, Y. Ōnuki, J. Phys. Soc. Jpn. 65 (Suppl. B) (1996) 202.
[18] Y. Machida, A. Itoh, Y. So, K. Izawa, Y. Haga, E. Yamamoto, N. Kimura, Y. Ōnuki, Y. Tsutsumi, K. Machida, Phys. Rev. Lett. 108 (2012) 157002.
[19] R. Settai, T. Takeuchi, Y. Ōnuki, J. Phys. Soc. Jpn. 76 (2007) 051003.

[20] Y. Matsuda, H. Shimahara, J. Phys. Soc. Jpn. 76 (2007) 051005.
[21] T. Tayama, A. Harita, T. Sakakibara, Y. Haga, H. Shishido, R. Settai, Y. Ōnuki, Phys. Rev. B 65 (2002) 180504(R).
[22] F. Honda, R. Settai, D. Aoki, Y. Haga, T.D. Matsuda, N. Tateiwa, S. Ikeda, Y. Homma, H. Sakai, Y. Shiokawa, E. Yamamoto, A. Nakamura, Y. Ōnuki, J. Phys. Soc. Jpn. 77 (Suppl. A) (2008) 339.
[23] H. Yamagami, D. Aoki, Y. Haga, Y. Ōnuki, J. Phys. Soc. Jpn. 76 (2007) 083708.
[24] Y. Nakano, F. Honda, T. Takeuchi, K. Sugiyama, M. Hagiwara, K. Kindo, E. Yamamoto, Y. Haga, R. Settai, H. Yamagami, Y. Ōnuki, J. Phys. Soc. Jpn. 79 (2010) 024702.
[25] Y. Haga, D. Aoki, T.D. Matsuda, K. Nakajima, Y. Arai, E. Yamamoto, A. Nakamura, Y. Homma, Y. Shiokawa, Y. Ōnuki, J. Phys. Soc. Jpn. 74 (2005) 1698.
[26] T. Maehira, T. Hotta, K. Ueda, A. Hasegawa, Phys. Rev. Lett. 90 (2003) 207007.
[27] F. Honda, M.-A. Measson, Y. Nakano, N. Yoshitani, E. Yamamoto, Y. Haga, T. Takeuchi, H. Yamagami, K. Shimizu, R. Settai, Y. Ōnuki, J. Phys. Soc. Jpn. 77 (2008) 043701.
[28] S. Ikeda, H. Shishido, M. Nakashima, R. Settai, D. Aoki, Y. Haga, H. Harima, Y. Aoki, T. Namiki, H. Sato, Y. Ōnuki, J. Phys. Soc. Jpn. 70 (2001) 2248, Errata; 70 (2001) 3187.
[29] J.L. Sarrao, L.A. Morales, J.D. Thompson, B.L. Scott, G.R. Stewart, F. Wastin, J. Rebizant, P. Boulet, E. Colineau, G.H. Lander, Nature (London) 420 (2002) 297.
[30] R. Settai, T. Kubo, T. Shiromoto, D. Honda, H. Shishido, K. Sugiyama, Y. Haga, T.D. Matsuda, K. Betsuyaku, H. Harima, T.C. Kobayashi, Y. Ōnuki, J. Phys. Soc. Jpn. 74 (2005) 3016.
[31] K. Oikawa, T. Kamiyama, H. Asano, Y. Ōnuki, M. Kohgi, J. Phys. Soc. Jpn. 65 (1996) 3229.
[32] D. Aoki, J. Flouquet, J. Phys. Soc. Jpn. 81 (2012) 011003.
[33] R. Settai, M. Nakashima, S. Araki, Y. Haga, T.C. Kobayashi, N. Tateiwa, H. Yamagami, Y. Ōnuki, J. Phys. Condens. Matter 14 (2002) L29.
[34] N. Tateiwa, K. Hanazono, T.C. Kobayashi, K. Amaya, T. Inoue, K. Kindo, Y. Koike, N. Metoki, Y. Haga, R. Settai, Y. Ōnuki, J. Phys. Soc. Jpn. 70 (2001) 2876.
[35] C. Pfleiderer, A.D. Huxley, Phys. Rev. Lett. 89 (2002) 147005.
[36] Y. Haga, M. Nakashima, R. Settai, S. Ikeda, T. Okubo, S. Araki, T.C. Kobayashi, N. Tateiwa, Y. Ōnuki, J. Phys. Condens. Matter 14 (2002) L125.
[37] I. Sheikin, A. Huxley, D. Braithwaite, J.-P. Brison, S. Watanabe, K. Miyake, J. Flouquet, Phys. Rev. B 64 (2001) 220503.
[38] N. Tateiwa, T.C. Kobayashi, K. Amaya, Y. Haga, R. Settai, Y. Ōnuki, Phys. Rev. B 69 (2004) 180513(R).
[39] H. Kusunose, Y. Kimoto, J. Phys. Soc. Jpn. 82 (2013) 094711.
[40] K. Satoh, S.W. Yun, I. Umehara, Y. Ōnuki, S. Uji, T. Shimizu, H. Aoki, J. Phys. Soc. Jpn. 61 (1992) 1827.
[41] A.B. Shick, W.E. Pickett, Phys. Rev. Lett. 86 (2001) 300.
[42] H. Yamagami, J. Phys. Condens. Matter 15 (2003) S2271.
[43] T. Terashima, T. Matsumoto, C. Terakura, S. Uji, N. Kimura, M. Endo, T. Komatsubara, H. Aoki, Phys. Rev. Lett. 87 (2001) 166401.
[44] T. Terashima, T. Matsumoto, C. Terakura, S. Uji, N. Kimura, M. Endo, T. Komatsubara, H. Aoki, K. Maezawa, Phys. Rev. B 65 (2002) 174501.
[45] K. Kubo, Phys. Rev. B 87 (2013) 195127.